

Reduced Order Spacecraft Charging Models for Electrostatic Proximity Operations

Julian Hammerl^{ID} and Hanspeter Schaub^{ID}

Abstract—Spacecraft charge in orbit due to naturally occurring electric currents from the ambient plasma emitted from the surface, as well as artificial currents produced by devices such as an electron gun. This results in electrostatic forces and torques between two spacecraft in close proximity that can perturb the relative motion and attitude during on-orbit servicing, assembly, and manufacturing (OSAM) operations. The forces and torques may also be utilized to remove or detumble dysfunctional satellites. In prior work on electrostatic proximity operations, typically charging models based on spherical spacecraft were used to compute the electrostatic potential, and that potential was prescribed to be constant in relative motion simulations. In this work, several charging models are compared for spacecraft with nonspherical shapes, including simple sphere models and faceted models. The faceted model is promising because its total surface area is more accurate, and it allows for the consideration of a time-varying sunlit area and ram-facing area. It is shown that the orientation of the spacecraft with respect to the Sun can significantly affect the equilibrium potential and the resulting force and torque. This is demonstrated by a charged attitude motion simulation for the electrostatic tractor (ET) debris removal concept. The effect of differential charging on the electrostatic force and torque is investigated. It is shown that differential charging can lead to significant force differences with respect to a fully conducting spacecraft, including a switch from repulsive to attractive force components.

Index Terms—Astrodynamics, electrostatics, proximity operations, relative motion, spacecraft charging.

I. INTRODUCTION

SPACECRAFT naturally build up electric potentials in orbit due to several electric currents in the space environment, such as the photoelectric current from the Sun or the electron and ion current from the ambient plasma [1, Ch. 1]. Spacecraft charging is usually not a concern in low Earth orbit (LEO) due to the dense and low-energy plasma, with the exception of a few distinct scenarios such as when a spacecraft is located at auroral latitudes during auroral activities. In high Earth orbit, such as geostationary Earth orbit (GEO) or cislunar

space, the plasma is tenuous and energetic, resulting in high electric potentials reaching tens of kilovolts in eclipse. Record charging events of up to -19 kV were experienced by the Applied Technology Satellite 6 (ATS-6) in GEO [2].

Spacecraft charging affects spaceflight in various ways. Even though modern spacecraft design guidelines recommend connecting all components to one common ground such that all components charge to the same potential [3, Ch. 3], this is not always possible and often not the case for old or retired satellites. Arcing can occur between two components of a satellite if they are charged to different potentials, which potentially reduces the lifetime of spacecraft [4], [5]. Electrostatic discharges can occur between two charged spacecraft during docking if the difference in electric potentials is large. One consequence of spacecraft charging that has received increased attention over the last decade is the electrostatic force that acts on two charged spacecraft in close proximity (see Fig. 1). Electrostatic perturbations can significantly influence on-orbit servicing, assembly, and manufacturing (OSAM) operations [6]. When an uncooperative target satellite is approached by a servicing satellite, the target starts to tumble due to the electrostatic torques if its center of mass is not aligned with its center of charge. The servicer needs to match this rotation to maintain a constant relative orientation with the target during rendezvous and docking. This increases fuel consumption and complicates servicing operations. The electrostatic forces and torques can also be utilized to remove space debris from geostationary orbit with the electrostatic tractor (ET) active debris removal method [7]. For the ET, a servicing satellite is equipped with an electron gun that is aimed at a retired satellite. Due to the emission of negatively charged electrons, the servicer charges positively, while the target object charges negatively due to the accumulation of electrons. The resulting attractive electrostatic force is then used to tug the target to a different orbit. In addition, the resulting electrostatic torque can be used to detumble uncooperative spacecraft [8].

Prior work on the effects of electrostatic perturbations on OSAM operations investigated adjusted approach trajectories that minimize the electrostatic torques and the resulting rotational rate of the target satellite [6]. A relative motion controller that feeds forward on the expected electrostatic perturbations to improve rendezvous performance was also studied [9]. However, all prior works prescribed electric potentials of -10 kV for each spacecraft assuming extreme charging scenarios [9], without considering the interactions of the spacecraft with the plasma environment. Spacecraft charging analysis has been done for the ET [10], [11]. The

Received 31 July 2024; revised 4 October 2024; accepted 7 November 2024. Date of publication 3 December 2024; date of current version 17 January 2025. This work was supported by U.S. Air Force Office of Scientific Research under Grant FA9550-20-1-0025 and Grant FA9550-23-1-0570. The work of Julian Hammerl was supported by National Aeronautics and Space Administration (NASA) Future Investigators in NASA Earth and Space Science and Technology (FINESST) Fellowship under Award 80NSSC22K1849. The review of this article was arranged by Senior Editor S. T. Lai. (Corresponding author: Julian Hammerl.)

The authors are with the Aerospace Engineering Sciences Department, University of Colorado at Boulder, Boulder, CO 80303 USA (e-mail: julian.hammerl@colorado.edu; hanspeter.schaub@colorado.edu).

Color versions of one or more figures in this article are available at <https://doi.org/10.1109/TPS.2024.3503356>.

Digital Object Identifier 10.1109/TPS.2024.3503356

0093-3813 © 2024 IEEE. Personal use is permitted, but republication/redistribution requires IEEE permission.
See <https://www.ieee.org/publications/rights/index.html> for more information.

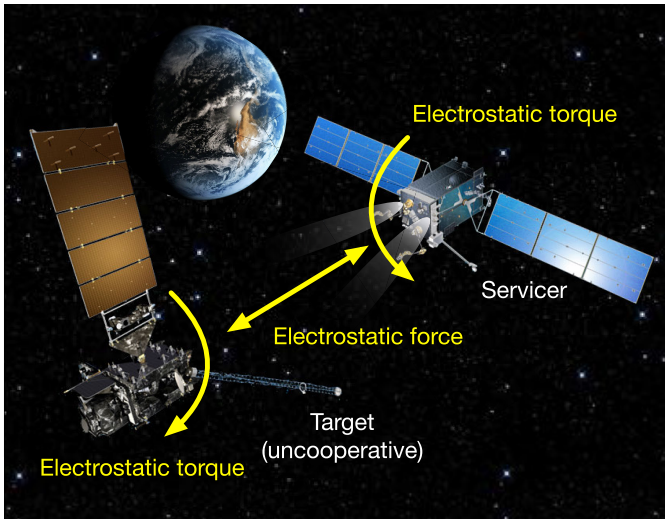


Fig. 1. Concept figure of electrostatic proximity operations.

effect of the debris attitude on the relative motion control, the electrostatic force, and, consequently, the reorbit performance has also been investigated [12], [13]. However, the effect of the debris attitude on the electric potential, which also affects the electrostatic force, has been neglected. The effect of Sun incidence angle on the electric potential and dynamics has been considered before, but only for individual lightweight Mylar debris that is subject to electromagnetic effects [14] and not for interspacecraft forces and torques during proximity operations. Finally, prior work on electrostatic proximity operations, both OSAM as well as active debris removal, assumed fully conducting spacecraft. The effects of differentially charged spacecraft on the intercraft electrostatic forces and torques have not been studied.

In this work, the electric potentials experienced by spacecraft in GEO and cislunar space are studied. To determine the equilibrium potential of satellites for science purposes or mission planning, numerical tools such as NASCAP-2k or SPIS are frequently used. Similar charging models are implemented here and utilized for the computation of electrostatic forces and torques. The first model assumes a spherical spacecraft. This is the simplest form of a charging model and cannot take into account the effect of the orientation of the spacecraft on the equilibrium potential. The other model divides the spacecraft into several facets while neglecting self-shadowing. This allows for an attitude-dependent computation of the equilibrium potential. With these models, the natural potentials in orbit around the Earth or Moon can be approximated, and the resulting electrostatic forces and torques are computed using the multisphere method (MSM) [15]. The electrostatic forces and torques during the ET reorbit process are studied using the faceted model. Finally, the effects of differential charging on the electrostatic forces and torques are investigated.

II. CHARGED SPACECRAFT FORCE MODELING

Various electric currents in the space environment cause spacecraft to charge in orbit. The plasma in space contains

electrons and ions that transfer their charge to the spacecraft upon impact [1, Ch. 1]. The resulting currents are referred to as the electron and ion plasma currents, respectively. As electrons and ions penetrate the surface material of the spacecraft, they transfer some of their energy to nearby electrons in the material. If enough energy is transferred, one or more secondary electrons (SEs) leave the surface material with low kinetic energies of a few electron-volts (eV), resulting in the so-called SE current [1, Ch. 3]. An incident electron can also be backscattered. In this case, an electron enters and leaves the surface material, resulting in the backscattered electron current [1, Ch. 3]. A spacecraft in sunlight is also subject to the photoelectric current. The incoming electromagnetic radiation from the Sun excites electrons in the surface material of the spacecraft that, similar to the SEs, leave the material with low energy [1, Ch. 7].

A. Spacecraft Charging Model

The charging model used here is taken from [16] and assumes a fully conducting spacecraft and orbit-limited attraction of the plasma particles. With the orbit-limited approximation for the plasma currents, the environmental plasma electron and ion flux of a nonspherical-shaped spacecraft are assumed to be equal to the fluxes incident on a sphere with the same potential [17]. In other words, the plasma electron and ion currents for a nonspherical spacecraft are assumed to be equal to those for a spherical spacecraft with the same surface area and potential. For orientation-dependent currents, such as the photoelectric current, a faceted model is used to accurately compute the Sun-facing area for example. It is assumed that the only coupling of the charging dynamics between the two spacecraft is due to the electron beam. A highly charged spacecraft causes changes in the ambient plasma, which affects the potential of a nearby spacecraft. In addition, a positively charged servicer attracts secondary and photoelectrons generated from a negatively (or less positively) charged target, resulting in a target spacecraft that is charged more positively than one would expect according to the isolated charging model used in this work. The consideration of such coupled effects is left for future work.

The following currents are considered using the potential of the target ϕ_T , the potential of the servicer ϕ_S , and a general spacecraft potential ϕ (as a placeholder for either ϕ_T or ϕ_S):

- 1) plasma electron current, $I_e(\phi)$;
- 2) plasma ion current, $I_i(\phi)$;
- 3) photoelectric current, $I_{ph}(\phi)$;
- 4) plasma electron-induced secondary and backscattered electron current, $I_{SEE,B,e}(\phi)$;
- 5) plasma ion-induced SE current, $I_{SEE,i}(\phi)$;
- 6) electron beam current on target $I_{EB,T}(\phi_T, \phi_S)$ and servicer $I_{EB,S}(\phi_T, \phi_S)$;
- 7) electron beam-induced secondary and backscattered electron current, $I_{SEE,B,eb}(\phi_T, \phi_S)$ (only on target).

The photoelectric current is attitude-dependent unless the spacecraft is eclipsed, and the plasma ion current may also change with attitude under certain conditions. Thus, they are

highlighted here for convenience. The plasma ion current is modeled as

$$I_i(\phi) = \begin{cases} \frac{A_p q_e n_i w_i}{4} \left(1 - \frac{\phi}{T_i}\right), & \text{if } w_i \geq v_{i,\text{bulk}}, \phi \leq 0 \\ \frac{A_p q_e n_i w_i}{4} e^{-\phi/T_i}, & \text{if } w_i \geq v_{i,\text{bulk}}, \phi > 0 \\ A_{\text{ram}} q_e n_i v_{i,\text{bulk}}, & \text{if } w_i < v_{i,\text{bulk}} \end{cases} \quad (1)$$

with the area A_p of the spacecraft that is exposed to the plasma (surface area), elementary charge q_e , ion density n_i in units of m^{-3} , ion temperature T_i in units of eV, and the thermal ion speed $w_i = (8T_i/(m_i\pi))^{1/2}$. The ion mass m_i is assumed to be equal to the proton mass m_p . The first two cases represent the attracting and repelling conditions, respectively, depending on the potential of the spacecraft. The third case represents a mesothermal environment when the bulk speed $v_{i,\text{bulk}}$ (the directional flow speed) of the ions with respect to the spacecraft is greater than the thermal speed w_i of the ions. In mesothermal conditions, the ions impact only on the ram side of the spacecraft. The ram-side area A_{ram} is attitude-dependent unless the spacecraft is spherical. Thus, in this case, the plasma current depends on attitude but not potential. In a mesothermal environment, the ions may be collected from an area that is larger than simply the cross-sectional area when the spacecraft is negatively charged [18], [19]. Particle-in-cell simulations are required to determine this increased ion collection. Such enhancement is neglected here but recommended for future work that focuses on the effects of spacecraft-induced plasma wakes. Examples of mesothermal environments are LEO (high spacecraft speed but low ion energies) and some cislunar regions (high ion bulk speed).

The photoelectric current is equal to

$$I_{\text{ph}}(\phi) = \begin{cases} j_{\text{ph},0} A_{\text{ph}}, & \text{if } \phi \leq 0 \\ j_{\text{ph},0} A_{\text{ph}} e^{-\phi/T_{\text{ph}}}, & \text{if } \phi > 0 \end{cases} \quad (2)$$

where $j_{\text{ph},0}$ and T_{ph} are the flux and temperature of the emitted photoelectrons and A_{ph} is the sunlit area of the spacecraft. Values of $j_{\text{ph},0} = 20 \mu\text{A}/\text{m}^2$ and $T_{\text{ph}} = 2 \text{ eV}$ are used in this work [10]. Photoelectrons are emitted with very low energy, so, for a positively charged spacecraft, the photoelectric current drops off exponentially. Similar to the ram-side area, the sunlit area is also attitude-dependent unless the spacecraft is spherical.

The total current on the target is

$$I_{\text{tot},T}(\phi_T, \phi_S) = I_e(\phi_T) + I_i(\phi_T) + I_{\text{ph}}(\phi_T) + I_{\text{SEE},B,e}(\phi_T) + I_{\text{SEE},i}(\phi_T) + I_{\text{EB},T}(\phi_T, \phi_S) + I_{\text{SEE},B,eb}(\phi_T, \phi_S) \quad (3)$$

and the total current on the servicer is

$$I_{\text{tot},S}(\phi_T, \phi_S) = I_e(\phi_S) + I_i(\phi_S) + I_{\text{ph}}(\phi_S) + I_{\text{SEE},B,e}(\phi_S) + I_{\text{SEE},i}(\phi_S) + I_{\text{EB},S}(\phi_T, \phi_S) \quad (4)$$

The equilibrium potentials are determined by finding the root of these equations. Due to the electron beam, the charging dynamics of the two spacecraft are coupled, and the individual total currents are a function of both spacecraft

potentials ϕ_T and ϕ_S . The most straightforward way is to compute the equilibria sequentially by finding the root of each equation individually: the equilibrium potential of the servicer ϕ_S is determined first with (4), assuming a target potential of 0 V (this assumption is discussed and justified in [16]). Now that the servicer potential is known; it is used to solve for the target potential ϕ_T using (3). Alternatively, a bivariate root-finding algorithm can be used to find the equilibrium potentials using the equation $I_{\text{sum}}(\phi_T, \phi_S) = (I_{\text{tot},T}(\phi_T, \phi_S)^2 + I_{\text{tot},S}(\phi_T, \phi_S)^2)^{1/2}$ [16]. As described thoroughly in [16], multiple equilibria (roots) may exist with an active electron beam, requiring bivariate root-finding algorithms or simulations to determine the converged potentials. In this work, the equilibria potentials are determined sequentially.

B. Multisphere Method

The MSM uses several spheres to approximate the charge distribution of complex shapes and is implemented here to calculate the electrostatic force and torque acting on each spacecraft [15], [20]. The voltage-to-charge relation is given by

$$\begin{bmatrix} V_1 \\ V_2 \\ \vdots \\ V_n \end{bmatrix} = k_c \begin{bmatrix} 1/R_1 & 1/r_{1,2} & \cdots & 1/r_{1,n} \\ 1/r_{2,1} & 1/R_2 & \cdots & 1/r_{2,n} \\ \vdots & \vdots & \ddots & \vdots \\ 1/r_{n,1} & 1/r_{n,2} & \cdots & 1/R_n \end{bmatrix} \begin{bmatrix} Q_1 \\ Q_2 \\ \vdots \\ Q_n \end{bmatrix} \quad (5)$$

or

$$\mathbf{V} = [\mathbf{S}]\mathbf{Q} \quad (6)$$

where V_i , Q_i , and R_i are the electric potential, electric charge, and radius of the i th sphere, respectively; $r_{i,j}$ is the distance between the i th and j th sphere; and k_c is the Coulomb constant. The matrix $[\mathbf{S}]$ is known as the elastance matrix, which is the inverse of the capacitance matrix [20]. Knowing the charge on each sphere, the electrostatic force acting on spacecraft 1 is computed by

$$\mathbf{F}_1 = -k_c \sum_{j=1}^{n_1} \mathbf{Q}_{1j} \left(\sum_{i=1}^{n_2} \frac{\mathbf{Q}_{2i}}{r_{i,j}^3} \mathbf{r}_{i,j} \right) \quad (7)$$

and the electrostatic torque acting on spacecraft 1 about point 0 is computed by

$$\mathbf{L}_{1,0} = -k_c \sum_{j=1}^{n_1} \mathbf{r}_j \times \mathbf{Q}_{1j} \left(\sum_{i=1}^{n_2} \frac{\mathbf{Q}_{2i}}{r_{i,j}^3} \mathbf{r}_{i,j} \right). \quad (8)$$

In the equations above, \mathbf{Q}_1 includes the charges of the n_1 spheres of spacecraft 1, \mathbf{Q}_2 includes the charges of the n_2 spheres of spacecraft 2, and \mathbf{r}_j is the vector from the point 0 to the j th sphere. The multisphere models used in this work are shown in Fig. 2. The target is based on the GOES-R satellite and is interesting due to its asymmetric shape, while the servicer is based on an SSL-1300 satellite bus. Previous work shows that a model with 20 spheres per spacecraft, distributed on the surface, provides a good representation of the electrostatic forces while requiring about 1/6 of the computational effort than a model with 80 spheres

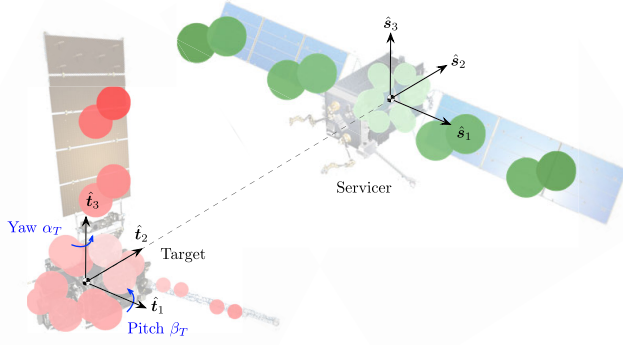


Fig. 2. Multisphere spacecraft models. Target spacecraft on the left, servicing spacecraft on the right.

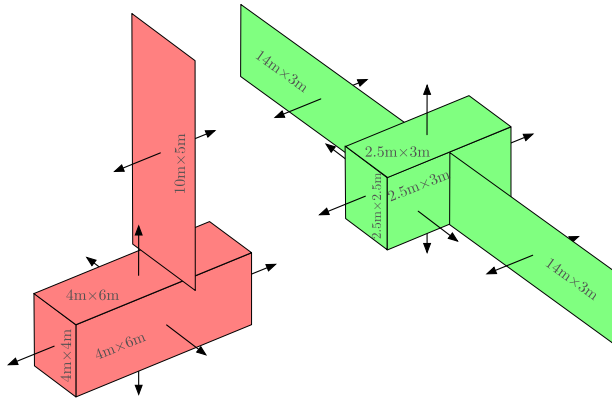


Fig. 3. Faceted spacecraft model.

per spacecraft [12]. Fig. 2 also shows the body frame of the target $\mathcal{T} : \{\hat{t}_1, \hat{t}_2, \hat{t}_3\}$ and the servicer $\mathcal{S} : \{\hat{s}_1, \hat{s}_2, \hat{s}_3\}$ in their nominal orientation. A 3-2-1 Euler rotation sequence with yaw angle α_T and pitch angle β_T is used to describe the orientation of the target. A roll rotation about the \hat{t}_2 axis is assumed not to provide any additional insight because the important orientations such as the solar panel facing (or not facing) the Sun and the solar panel pointing (or not pointing) at the servicer are covered using only yaw and pitch. Thus, the rotation of this axis is always set to zero to improve the visualization of the results by using only two rotation angles. The orientation shown in the figure has both frames aligned with the Hill frame. For any rotation of either spacecraft, the Hill frame is used as a reference.

C. Faceted Charging Model

A faceted charging model is implemented to compute the projected sunlit area and ram-side area of the spacecraft, neglecting self-shadowing. Self-shadowing refers to the shadowing of components by other components of the individual spacecraft. In terms of one spacecraft shadowing the other, it is assumed that if that is the case, the entire shadowed spacecraft is in eclipse. Shadowing of part of a spacecraft by the other spacecraft is not considered. The spacecraft is divided into n facets with area A_i and normal vector \hat{n}_i of the i th facet. The

projected sunlit area of the i th facet is equal to

$$A_{\text{ph},i} = \begin{cases} A_i \cos \theta_{s,i} = A_i \frac{\hat{s} \cdot \hat{n}_i}{|\hat{s}| \cdot |\hat{n}_i|}, & \text{if } \hat{s} \cdot \hat{n}_i > 0 \\ 0, & \text{if } \hat{s} \cdot \hat{n}_i \leq 0 \end{cases} \quad (9)$$

where $\theta_{s,i}$ is the angle between the Sun direction \hat{s} and the normal to the surface \hat{n}_i . If the dot product $\hat{s} \cdot \hat{n}_i$ is negative, the area is facing away from the Sun, so the sunlit area for that facet is set equal to 0. The total projected area of the spacecraft that is facing the Sun is then

$$A_{\text{ph}} = \sum_{i=1}^n A_{\text{ph},i}. \quad (10)$$

Similarly, the projected ram-side area of the i th facet is equal to

$$A_{\text{ram},i} = \begin{cases} A_i \cos \theta_{v,i} = A_i \frac{\hat{v}_r \cdot \hat{n}_i}{|\hat{v}_r| \cdot |\hat{n}_i|}, & \text{if } \hat{v}_r \cdot \hat{n}_i > 0 \\ 0, & \text{if } \hat{v}_r \cdot \hat{n}_i \leq 0 \end{cases} \quad (11)$$

where $\theta_{v,i}$ is the angle between the spacecraft's direction of motion with respect to the ion flow

$$\hat{v}_r = \frac{\mathbf{v}_{S/C} - \mathbf{v}_{\text{bulk}}}{|\mathbf{v}_{S/C} - \mathbf{v}_{\text{bulk}}|} \quad (12)$$

with the spacecraft velocity $\mathbf{v}_{S/C}$ and the ion bulk velocity \mathbf{v}_{bulk} (the direction of the ion flow). If the dot product $\hat{v}_r \cdot \hat{n}_i$ is negative, the area is facing away from the ion flow so the ram-side area for that facet is set equal to 0. The total projected ram-side area of the spacecraft is then

$$A_{\text{ram}} = \sum_{i=1}^n A_{\text{ram},i}. \quad (13)$$

Fig. 3 shows the faceted models for the GOES-R and SSL-1300 spacecraft, including the dimensions and normal vectors of the facets.

The implemented charging model is compared with NASCAP-2k for $n_e = 5 \cdot 10^4 \text{ m}^{-3}$, $T_e = 3700 \text{ eV}$, $n_i = 6.9 \cdot 10^4 \text{ m}^{-3}$, $T_i = 4800 \text{ eV}$, and $j_{\text{ph},0} = 40 \mu\text{A}/\text{m}^2$ by calculating the equilibrium potential and all relevant currents for the target. In this comparison, the target \hat{t}_2 axis is facing the Sun, and all currents are computed for the equilibrium potential of 10.98 V as obtained by Nascap. The results are shown in Table I. The main deviation comes from the different SE yield models implemented, which are relatively uncertain and depend on many factors, such as surface material, roughness, and level of oxidation [21].

III. CISLUNAR SPACE STUDY

Due to the low GEO orbital speed of the spacecraft and high ion temperatures, the ion thermal speed is greater than the ion bulk speed, and consequently, the plasma ion current is assumed to be independent of the spacecraft's attitude and speed. In LEO, the ion bulk speed in the spacecraft reference frame is greater than the ion thermal speed, so charging does depend on the spacecraft's orientation. However, due

TABLE I
COMPARISON BETWEEN NASCAP-2K AND IMPLEMENTED CHARGING MODEL

Model	Eq. Pot. [V]	I_e [μA]	I_i [μA]	$I_{SEE,B,e}$ [μA]	$I_{SEE,i}$ [μA]	I_{ph} [μA]
NASCAP-2k	10.980	-18.644	0.680	7.053	0.004	10.910
Ref. [16]	10.122	-18.643	0.680	0.930	0.102	10.898

to electrostatic shielding and low electrostatic potentials, intercraft electrostatic forces and torques are much smaller in LEO [22], [23]. In lunar orbit, the plasma temperatures and the ion bulk speed depend on the location of the Moon with respect to the magnetic field of the Earth. Four regimes are defined for spacecraft charging in cislunar space, as described in the NASA design specification for natural environments (DSNE) [24]: plasma sheet, magnetotail lobes, magnetosheath, and solar wind. Depending on space weather and the regime that the spacecraft is located in, the ion bulk speed may be greater than the ion thermal speed, and consequently, ram-side ion collection may apply. The electron and ion density and temperature, as well as ion bulk speed, are provided in DSNE for each regime. In the plasma sheet and magnetotail lobes regimes, the plasma properties are assumed to be the same for all altitudes above the Moon, regardless of whether the spacecraft is on the Sun-facing or eclipsed side of the Moon. In the magnetosheath and solar wind regimes, the plasma properties are provided individually for various altitude regions. In addition, a plasma wake exists in these regimes on the downwind side of the Moon due to the obstruction of the solar wind flow [25], [26], [27]. Thus, another differentiation for the plasma parameters is made in these regimes depending on whether the spacecraft is on the Sun-facing (day-side) or eclipsed side (wake-side or night-side) of the Moon. The mean and max of the plasma parameters are provided in DSNE, and the max is used in this work to represent a high-charging environment. The cislunar plasma parameters used in this work are summarized in Table II.

Using the plasma data from DSNE and the faceted spacecraft model from Section II, the natural potentials are computed for the target for several spacecraft's orientations with the given charging model and shown in Fig. 4. The minimum, maximum, and average equilibrium potentials across all orientations are recorded. Due to the high electron temperatures, the average natural equilibrium potential obtained for the plasma sheet is -7.64 kV. The range of potentials, depending on the spacecraft's orientation, is between about -10.5 and -6 kV. If the target \hat{t}_2 is perpendicular to the ion flow, the ram-side area is the smallest, and consequently, the equilibrium potential is the most negative due to the reduced plasma ion current. The potential of -6 kV is obtained when the target \hat{t}_2 is facing the same way as the ion flow, as this results in the maximum ram-side area for the given faceted model. In the magnetotail lobes, the ion thermal speed is greater than the ion bulk speed, so ram-side charging does not apply. The electron temperature is too low for the onset of charging, so the equilibrium potential is about 1 V positive for all orientations. In the magnetosheath regime, ram-side charging applies on the day-side and in the higher altitudes of the night-side, resulting

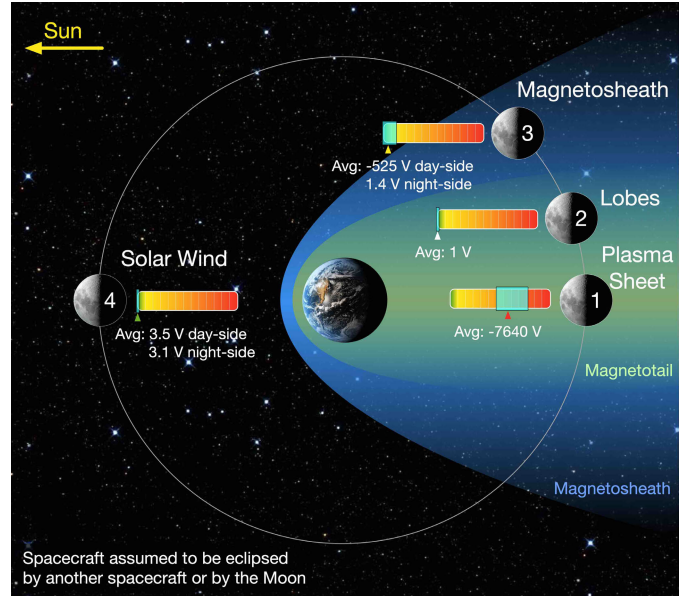


Fig. 4. Natural potentials in cislunar space for an eclipsed spacecraft, obtained using a faceted model of the target. The teal area indicates the range of equilibrium potentials, depending on the spacecraft's orientation. The average equilibrium potential across all orientations is also indicated.

in equilibrium potentials between -1.5 and 0 kV and an average of about -0.5 kV on the day-side. No significant charging occurs on the night side due to a lower electron temperature. Similarly, in the solar wind regime, ram-side charging applies on the day-side and in the higher altitudes of the night-side. Because the electron temperature here is low across all altitudes and on both sides of the Moon, the obtained equilibrium potentials are just slightly positive both on the day and night side.

Although more detailed spacecraft models and higher order charging models are needed to estimate the possible charging levels of mission-specific satellites, the reduced-order charging model used here provides a qualitative study. In terms of electrostatic OSAM operations, the electrostatic perturbations resulting from spacecraft charging are considered to be the most concerning in the plasma sheet and the magnetosheath.

IV. ET FACETED MODEL ANALYSIS

The photoelectric effect provides a strong, naturally occurring current in the space environment that is scaled by the sunlit area of the spacecraft. If a spherical shape is used for the charging model, the sunlit area is independent of the orientation. However, for more complex shapes such as satellites, the sunlit area can vary significantly. The faceted model described earlier is implemented to account for these variations. The plasma parameters used here correspond to a local time of $LT = 12$ h in geostationary orbit and a

TABLE II
CISLUNAR PLASMA PARAMETERS (TAKEN FROM [24])

Region	Electron Density [m^{-3}]	Electron Temp. [eV]	Ion Speed [km/s]	Ion Density [m^{-3}]	Ion Temp. [eV]
Magnetotail Lobes >100 km	6.2E+04	980	650	8.9E+04	3400
Plasma Sheet >100 km	5.0E+04	3700	1100	6.9E+04	4800
Magnetosheath Dayside >100 km	7.6E+04	1400	930	9.9E+04	3000
Magnetosheath Wake 100 km - 2000 km	4.3E+04	840	660	5.0E+04	3600
Magnetosheath Wake 2000 km - 12000 km	6.6E+04	920	770	9.2E+04	2900
Magnetosheath Wake >12000 km	7.7E+04	710	820	1.3E+05	1800
Solar Wind Dayside >100 km	6.6E+07	126	730	7.0E+07	121
Solar Wind Wake 100 km - 500 km	2.3E+04	430	720	3.6E+04	2300
Solar Wind Wake 500 km - 2000 km	5.0E+04	350	770	6.5E+04	2500
Solar Wind Wake 2000 km - 12000 km	3.5E+04	220	770	4.8E+04	2100
Solar Wind Wake >12000 km	1.5E+06	64	790	1.4E+06	800

planetary K-index of $K_p = 2$ according to [28] and are equal to $n_e = 6 \cdot 10^5 \text{ m}^{-3}$, $T_e = 700 \text{ eV}$, $n_i = 6.5 \cdot 10^5 \text{ m}^{-3}$, and $T_i = 8000 \text{ eV}$. The plasma being slightly nonneutral is a result of how the energetic particles arrive in geostationary orbit. The energetic electrons and ions in GEO typically come from the magnetotail. As they arrive at Earth, electrons travel eastward (into the dawn region) and ions travel westward (into the dusk region) due to Earth's magnetic field [1]. This results in a reduced electron density compared to the ion density in the dusk region. Denton et al. [28] show that this low electron/ion density ratio can extend into the noon region. An electron beam is included with an energy of $E_{EB} = 30 \text{ keV}$ and a current of $I_{EB} = 1 \text{ mA}$. The spacecraft centers are 15 m apart, with their nominal orientation shown in Fig. 2, and the Sun direction is aligned with the nominal \hat{t}_1 direction.

Fig. 5 shows the equilibrium potential of the GOES-R target satellite as a function of its orientation, as obtained with the faceted model. The orientation of the target is changed using yaw and pitch 3-2-1 Euler rotations, as depicted in Fig. 2, while the servicer remains at the nominal orientation. For orientations where the yaw angle is close to $\alpha_T = \{-180^\circ, 0^\circ, 180^\circ\}$ or the pitch angle is close to $\beta_T = \{-90^\circ, 90^\circ\}$, the equilibrium potential is highly negative, while it is approximately zero for all other orientations. The aforementioned angles correspond to those orientations where the solar panel of the GOES-R satellite is edge-on with the Sun, that is, the normal vectors of the two panel facets are (nearly) perpendicular to the Sun direction \hat{s} . If the solar panel normal vector is more aligned with the Sun direction, the sunlit area is increased, providing a greater photoelectric current. Because the released photoelectrons are attracted back to the spacecraft once it is positively charged, the target settles to an equilibrium potential that is only a few volts positive (close to zero). The equilibrium potential of the servicer is about +7 kV due to the electron beam current. It should be noted that a roll rotation about the \hat{t}_2 axis also affects the resulting potential, force, and torque. As described in Section II, it is neglected here because the most important orientations are covered using only yaw and pitch.

To study the effect of the orientation-dependent equilibrium potential on electrostatic proximity operations, four different models are considered to compute the electrostatic force and torque as a function of the target orientation. The highest-fidelity model uses the faceted model to compute the electric

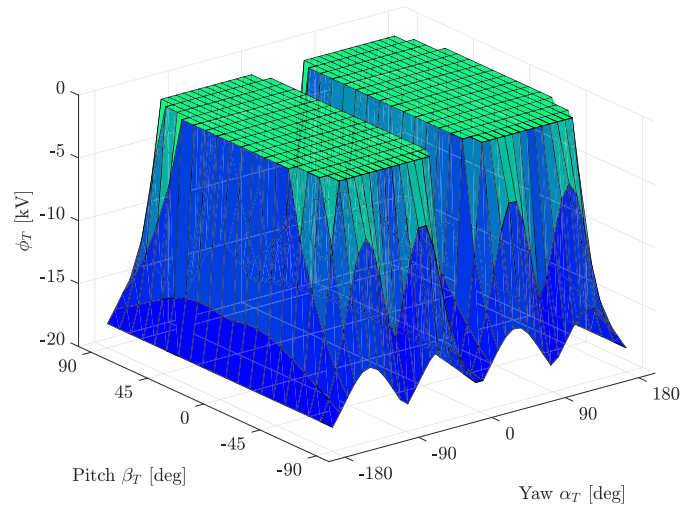


Fig. 5. Electric potential of the target ϕ_T as function of target orientation.

potential of the spacecraft and the multisphere model (MSM) to calculate the resulting force and torque (Model 1—“faceted, MSM”), while the lowest-fidelity model uses a spherical spacecraft to determine the potential and a one-sphere model (ISM) to approximate the force and torque (Model 4—“spherical, ISM”). Two more models are studied that are a mix of the highest and lowest fidelity models (Model 2—“spherical, MSM”; Model 3—“faceted, ISM”). The radius R_{eff} of the single sphere is chosen to match the self-capacitance C of the MSM model

$$R_{\text{eff}} = \frac{C}{4\pi\epsilon_0} \quad (14)$$

where ϵ_0 is the vacuum permittivity. This radius is referred to as the effective radius and is equal to 4.4438 m for the GOES-R and 4.7984 m for the SSL-1300 satellite. Essentially, the faceted model accounts for the effect of the orientation on the equilibrium potential (which affects the force and torque), while the MSM model accounts for the direct effect of the orientation on the electrostatic force and torque.

Fig. 6 shows the electrostatic force between the servicer and target as a function of the target orientation for the different models. There are three clear peaks in force magnitude for the highest-fidelity model. These peaks also exist for the “spherical, MSM” model and are consequences of the solar

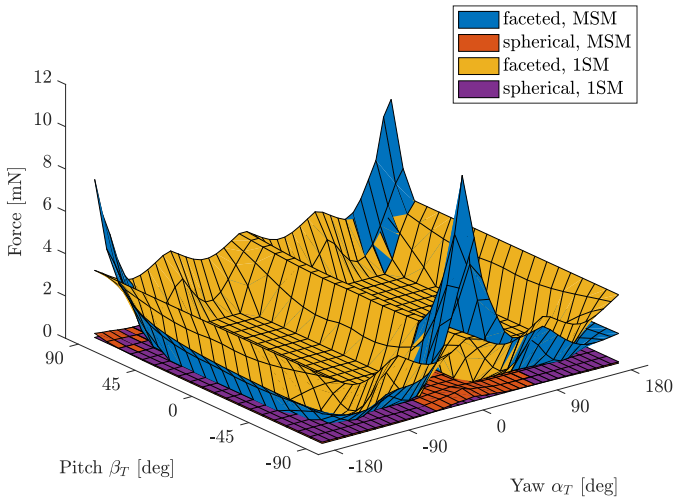


Fig. 6. Electrostatic force magnitude as a function of target orientation using different models.

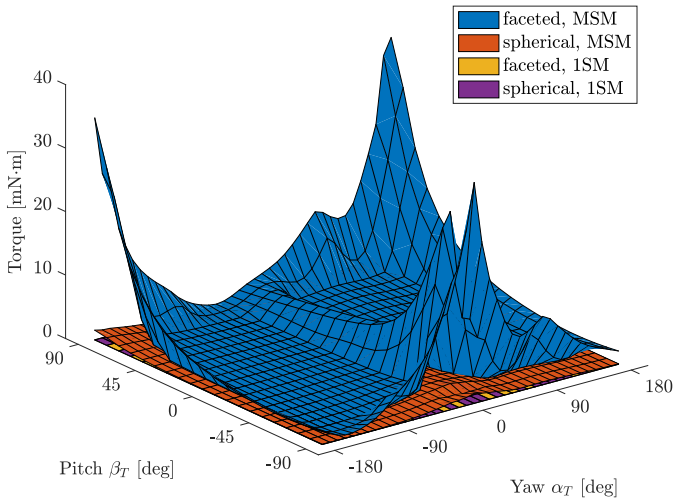


Fig. 7. Electrostatic torque magnitude as a function of target orientation using different models.

panel of the target pointing toward the servicer. However, this effect is pronounced for the highest-fidelity model because the solar panel is edge-on with the Sun for these orientations, leading to a more negative electric potential that further increases the electrostatic force. The force magnitude for the “faceted, 1SM” model essentially corresponds to Fig. 5 but flipped upside down. When the electric potential is more negative, the force is greater due to the positively charged servicing spacecraft. Finally, the force for the “spherical, 1SM” model is constant across all orientations.

The electrostatic torque as a function of yaw and pitch angles is shown in Fig. 7. For the one-sphere models (Models 3 and 4), the torque is zero across all orientations because the center of charge is always aligned with the center of mass for a single sphere, producing no torque. The observations for the torque of the MSM models (Models 1 and 2) are similar to the observations above for the force magnitude. Model 2 accounts for the torque variations due to different orientations, but, for the given GOES-R spacecraft model, these variations are enhanced by the orientation-dependent equilibrium potential.

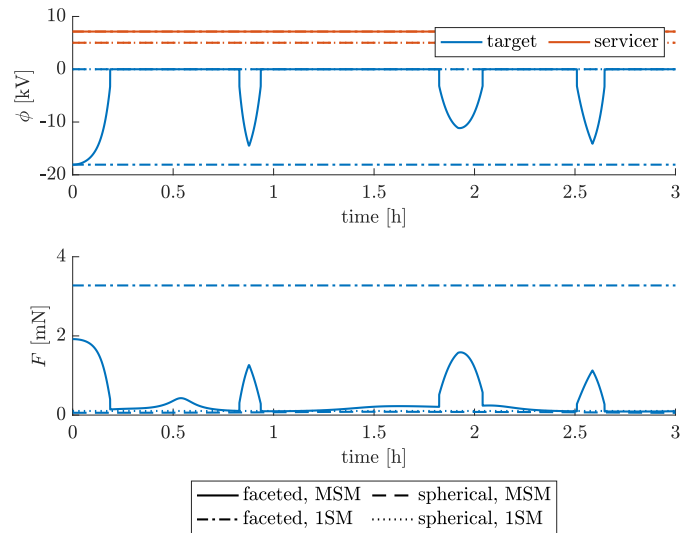


Fig. 8. Electric potential ϕ of target and servicer and force magnitude F over time during the ET debris reorbit scenario.

A rotational dynamic simulation is performed, where the relative position of the two spacecraft and the attitude of the servicer are held constant, but the target satellite is free to rotate given the electrostatic torque that is acting on it (see Fig. 8). The rotational dynamics of the target are given by [29, Ch. 4]

$$[I_T]\dot{\omega} = -[\tilde{\omega}][I_T]\omega + L_c \quad (15)$$

where $[I_T]$ is the inertia matrix of the target, ω is the angular velocity of the target, and L_c is the electrostatic torque acting on the target. The skew-symmetric matrix $[\tilde{\omega}]$ is used as the cross-product equivalent matrix operator of ω . The inertia matrix is obtained from a CAD model of the target that is generated using publicly available size and mass information of a GOES-R satellite [30].

The initial attitude corresponds to the nominal orientation shown in Fig. 2 with zero angular velocity. Due to the electrostatic torque, the target starts rotating. Because the one-sphere model cannot account for any torques if the center of mass is at the center of the sphere, the orientation of the target stays constant throughout the simulation, and neither the potential nor the force changes. In the case of the “faceted, 1SM” model, the potential remains at about -18 kV because the sunlit area of the faceted model at its initial (and in this case constant) orientation is rather small, causing a strong force, but no torque.

The cases of the multisphere models are more interesting. Due to the large cross section of the 4.4438-m radius GOES-R effective sphere that is facing the Sun, the equilibrium potential is about 0 V for the “spherical, MSM” model, at all times. Regardless of the 0-V potential, the electrostatic force and torque are nonzero due to induced charging effects [31]. The force and torque are rather small in magnitude, so the rotational rate of the target is small as well. Finally, the “faceted, MSM” model provides the most detail as it is the highest-fidelity model used here. Initially, the potential of the target spacecraft is at about -18 kV. As the target

starts rotating due to the electrostatic torque, the sunlit area increases, which makes the equilibrium potential less negative. At some point, the potential is close to zero, and the force is significantly lower than at the beginning. After about 0.8 h, only a small area of the target spacecraft is in sunlight once again, causing a spike in the equilibrium potential and the electrostatic force. The differences between these models depend on the specific shapes of the spacecraft, but the results demonstrate that the charge distribution and dynamics can be misrepresented by a spherical, one-sphere model.

These results have two main implications for the ET debris removal method. First, the electron beam current I_{EB} must be sufficiently high to charge the debris regardless of the orientation of the debris. In the example used here, the beam current is not sufficiently high, causing debris potentials of only a few volts for those orientations where the photoelectric current is the strongest. This results in large force fluctuations throughout the reorbit process that directly affect the time needed to reorbit the debris. Second, although one of the advantages of the ET compared to other proposed active debris removal methods is that it is not required to detumble the retired satellite before reorbiting, the results from this work suggest that detumbled debris may be beneficial. In [12], it was found that the sensitivity of the ET relative motion control to the uncertainty of the debris electric potential is higher for some orientations than others. The following work demonstrated that this sensitivity is averaged out if the debris is tumbling [13]. Although the variation of the force and the resulting change in reorbit time due to the varying debris orientation was taken into account in prior work, the potentially amplifying effect of the varying spacecraft potential on the electrostatic force and reorbit time was not considered. In addition to the fluctuating debris potential and electrostatic force, tumbling debris may introduce other complications, such as periodically differentially charged debris components as they move in and out of the shadow of the spacecraft, or relative navigation challenges. Thus, holding the debris at a favorable orientation, as discussed in [13], may be preferred. It is recommended for future work on the ET to investigate whether a tumbling or detumbled retired satellite is beneficial for the reorbit process and how to maintain a debris orientation using electrostatic torque control. It should also be noted that if the orientation of the debris with respect to the servicer remains constant while reorbiting, the inertial attitude and, consequently, the Sun-facing area and electric potential do change. Thus, it should be differentiated whether an inertially fixed or Hill frame fixed debris orientation is beneficial.

V. DIFFERENTIAL CHARGING ANALYSIS

The sensitivity of the electric potential to changes in the space environment and to the attitude of the spacecraft demonstrates the need for methods to estimate the electric potential of the servicer and target, which allows for the electrostatic force between the two neighboring spacecraft to be predicted. A Langmuir probe or retarding potential analyzer (RPA) may be used to measure the servicer potential [32], [33]. The target spacecraft is uncooperative or unable to measure its potential itself, so it is not as straightforward to

determine its electric potential remotely. Two methods have been studied for the remote estimation of electric potentials. One method is based on SEs and photoelectrons that are emitted from the target [34], [35], [36] due to the plasma environment and electromagnetic radiation from the Sun. Because these electrons are emitted with negligible kinetic energy and accelerated due to the electric field between the target and the servicer, one can infer the electric potential of the target by measuring the kinetic energy of these electrons as they arrive at the servicer. This method requires the target to be more negatively charged than the servicer. Otherwise, the SEs or photoelectrons are unable to reach the servicer. This is the case for the ET because the target is charged negative and the servicer positive. For OSAM operations, this method provides no measurement when the target is approximately neutral or the servicer charged more negatively than the target for example. The other method is based on X-rays that are excited by electrons impacting on the target [37], [38]. For the active X-ray method, the electrons come from an electron beam that is emitted from the servicer and aimed at the target. X-rays are only emitted up to the impact kinetic energy of the electrons. Due to the interaction of the electron beam with the electric field, the electric potential of the target is inferred by estimating the maximum X-ray energy in the recorded X-ray spectrum. Alternatively, the electric potential may also be estimated passively with X-rays that are excited by the ambient plasma environment [39]. For simplicity, it is often assumed that the target spacecraft is fully conducting, resulting in one single potential for the entire spacecraft. In [40] and [41], the electron method and the X-ray method are used to experimentally estimate the electric potential of differentially charged test objects, i.e., test objects with multiple components charged to different potentials. However, the effect of differentially charged spacecraft on the electric force between two neighboring spacecraft was not studied.

To study the electrostatic forces for differentially charged spacecraft, various potentials are prescribed to the bus and panel of the target and the servicer. The levels of the prescribed potentials are similar to the natural potentials obtained in Section III for the cislunar regions. The resulting force and torque are then computed as a function of the target orientation, as shown in Figs. 9 and 11. Assuming a fully conducting servicer, several conditions are considered according to the following representation key.

- 1) *Solid Surface*: Servicer in sunlight (potential of approximately 0 kV).
- 2) *Gridded Surface*: Servicer in eclipse (potential of approximately -5 kV).
- 3) *Black Surface*: Target is fully conducting in eclipse (potential of approximately -5 kV).
- 4) *Red Surface*: Target bus at 0 kV (B:0) and target panel at -5 kV (P: -5).
- 5) *Blue Surface*: Target bus at -5 kV (B: -5) and target panel at 0 kV (P:0).

A yellow surface is added to highlight the zero-crossing of the force or torque. In differential charging cases, the magnetometer of the target is always assumed to be at 0 V.

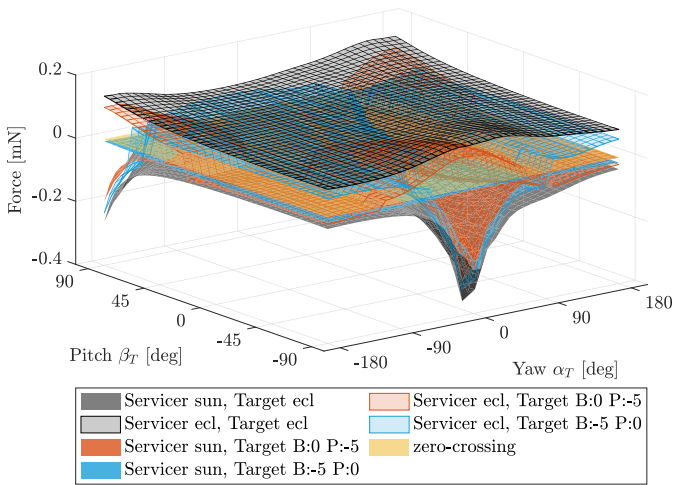


Fig. 9. Electrostatic force as a function of target orientation for the differentially charged target.

Possible reasons for these differential charging scenarios include varying material properties of the nonconducting spacecraft components and differences in exposure to sunlight. For example, consider a spacecraft with a potential of -5 kV (Section III). If some component is electrically not connected to the rest of the spacecraft and made of surface material with a higher SE yield, then that component charges less negatively or possibly even only a few volts positive due to the increased emission of negatively charged SEs. On the other hand, a partially eclipsed spacecraft may also differentially charge. Spacecraft in sunlight usually charge a few volts positive. If some electrically not-connected component is entirely on the shadowed side of the spacecraft, then it charges more negatively due to the missing photoelectric current [42], [43]. For more information, see [1, Ch. 6 and 7].

First, the electrostatic force is investigated in Fig. 9. Instead of simply plotting the (unsigned) magnitude of the force, the signed force magnitude is plotted to indicate whether the force is attracting or repelling the two spacecraft. The sign (“polarity”) p_F of the force is determined by looking at the component of the force along the direction from one spacecraft center to the other

$$p_F = \text{sign}(\mathbf{F}_{c,T} \cdot \mathbf{r}_{TS}) \quad (16)$$

where $\mathbf{F}_{c,T}$ is the electrostatic force acting on the target and \mathbf{r}_{TS} is the vector from the servicer center to the target center. A positive force corresponds to the repelling case, while a negative force corresponds to the attractive case.

If the servicer is in sunlight and the target is eclipsed (i.e., the servicer eclipses the target), the force is attractive (negative) and relatively small in magnitude for most target orientations because the servicer potential is approximately 0 kV. For those orientations where the target solar panel is pointed at the servicer, however, the force reaches a maximum magnitude of about 0.3 mN due to the small distance between the panel and the center of the servicer. If both spacecraft are eclipsed (for example, both spacecraft are behind the Moon), the force is repelling (positive). Although the force magnitude is also greater for orientations where the target panel comes

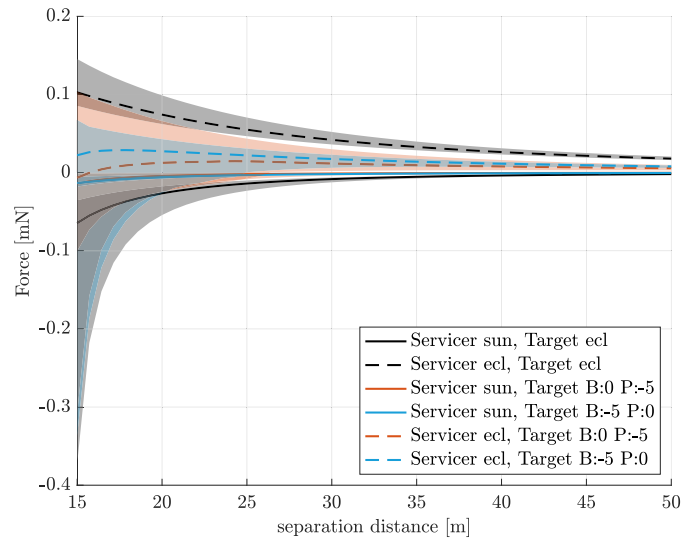


Fig. 10. Differential charging effects over various separation distances. The shaded regions represent the range of forces for all target orientations, while the lines themselves indicate the average force across all orientations.

closer to the servicer, the differences are not as significant as in the attractive case.

For the case where the servicer is in sunlight and the target is differentially charged, as shown by the solid red and blue surfaces in Fig. 9, the force magnitude is decreased with respect to the nondifferentially charged baseline scenario for a sunlit servicer (solid black surface). If the target bus is at 0 kV and the panel at -5 kV, the force dependence on attitude is qualitatively similar to the fully conducting target case. In contrast, if the bus is charged to -5 kV and the panel to 0 kV, there is barely any attitude dependence. This is because the panel, which is primarily responsible for the attitude effects, and the servicer are both at a potential of 0 kV, resulting in forces that are negligible compared to those between the servicer and the target bus. The attitude of the bus of the target, however, does not affect the electrostatic force as much.

The case where the servicer is eclipsed and the target is differentially charged is more interesting, represented by the gridded red and blue surfaces in Fig. 9. Regardless of which part of the target is at 0 or -5 kV, the polarity of the force becomes dependent on the orientation of the target. If the bus is at 0 kV and the panel at -5 kV, the force is repelling when the panel is directed at the servicer, similar to the scenario with an eclipsed servicer and fully conducting target, but attractive for some other orientations. If the bus is at -5 kV and the panel at 0 kV, the force is attractive when the panel is directed at the servicer, similar to the scenario with a sunlit servicer and fully conducting target, but repelling for most other orientations. This case is especially intriguing because the force magnitude is relatively large when the panel is pointing toward the servicer, but the force is of different polarity and actually more similar to the case of a sunlit servicer than the case of an eclipsed servicer (which is considered to be the baseline here). It should be noted again that the “polarity” of the force is simply determined by looking at the force component that

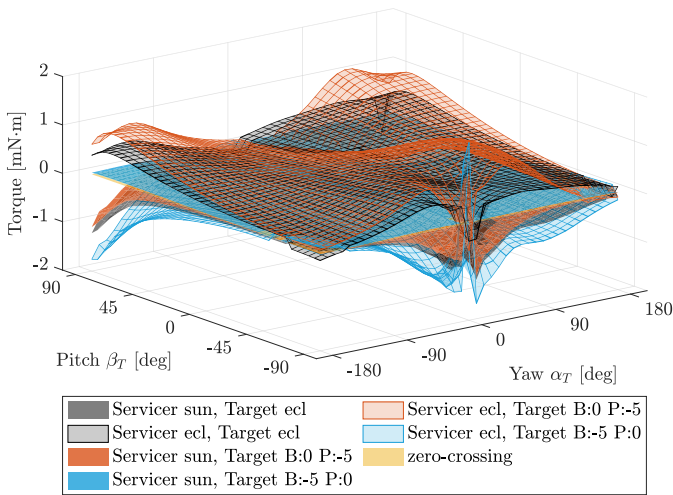


Fig. 11. Electrostatic torque on the target as a function of target orientation for the differentially charged target.

lies in the direction from one spacecraft center to the other. Thus, a switch in the polarity of the force only implies that this specific component of the force switches sign, while the other components may be unaffected.

Fig. 10 shows how the attitude effects decrease with increasing separation distance between the two spacecraft. The color scheme is the same as before, but here a solid line represents a sunlit servicer and a dashed line represents an eclipsed servicer. The shaded regions include the forces for all target orientations, and the lines themselves indicate the average force across all orientations for a given separation distance. At close separations, the attitude effects are relatively high, and the polarity of the force may switch between one orientation and another. Starting at about 25 m for the given spacecraft models and electric potentials, the polarity is the same for all orientations of one charging configuration. That is, the force polarity is not attitude-dependent for distances greater than about 25 m, and the target appears as fully conducting from a force perspective. This implies that the polarity of the force for a differentially charged spacecraft is also dependent on the separation distance. Increasing the separation distance even more causes the shaded regions to almost vanish. At those separations, the attitude dependence on the force is negligible, and the target appears as a fully conducting sphere from a force perspective.

Similar to the force, the electrostatic torque acting on the target is plotted in Fig. 11 for several charging cases as a function of the target orientation. To determine the sign (polarity) of the torque, a reference point is chosen on the target to compute the equivalent force acting on that point to generate that torque. This reference point is chosen to be approximately at the far end of the solar panel of the target, ${}^T\mathbf{r}_{PT} = [0, 0, 10]^T$ m, where the left superscript indicates that this vector is described in the target frame $\mathcal{T} : \{\hat{\mathbf{t}}_1, \hat{\mathbf{t}}_2, \hat{\mathbf{t}}_3\}$. The sign p_L of the torque is determined by looking at the component of the equivalent force acting on the reference point along the direction from one spacecraft center to the other

$$p_L = \text{sign}((\mathbf{L}_{c,T} \times \mathbf{r}_{PT}) \cdot \mathbf{r}_{TS}) \quad (17)$$

where $\mathbf{L}_{c,T}$ is the electrostatic torque acting on the target center of mass. A positive torque corresponds to the repelling case where the torque is pushing the panel of the target away from the servicer, while a negative torque corresponds to the attractive case where the torque is pulling the panel of the target toward the servicer. The torque on the target lies mostly in the $\hat{\mathbf{t}}_1 - \hat{\mathbf{t}}_2$ plane of the target frame because the panel of the given target spacecraft provides little torque leverage around $\hat{\mathbf{t}}_3$.

Many of the observations from the force study also apply to the torque study, but two findings stand out in Fig. 11. First, across all orientations, the force of the differentially charged target appears to be bounded by the two scenarios with a fully conducting target and the servicer either eclipsed or in sunlight. This is demonstrated in Fig. 9 as the blue and red surfaces do not pierce through the gridded or solid black surfaces. For a differentially charged spacecraft with the given potentials, the net force is reduced in magnitude. This is not the case for the torque, as is evident in Fig. 11. For some orientations, the electrostatic torque is actually enhanced due to differential charging. For example, if the servicer is eclipsed, a target spacecraft with a bus potential of 0 kV and panel potential of -5 kV experiences enhanced repulsive torques. The solar panel provides more leverage for the torque with respect to the center of mass, so the negative charge concentrated on the panel combined with the negatively charged servicer leads to higher repulsive torques. Similarly, with the bus at -5 kV, the panel at 0 kV provides more leverage for the attractive torque and, consequently, enhances the torque as well. The second finding is that the torque polarity of the differentially charged target may be switched with respect to the fully conducting target for almost all orientations, as opposed to only some specific orientations for the force polarity. The torque for an eclipsed servicer and fully conducting target is mostly repelling. However, if the target bus is negatively charged to -5 kV and the panel is at 0 kV, the resulting torque is attractive for almost all orientations. Although, for a given orientation, the force is repulsive, for example, the torque may be attractive due to the greater leverage of the panel.

Not only does differential charging of large spacecraft components affect the magnitude of the electrostatic force and torque but it can also lead to a switch of direction of the force component along the direction of separation. In addition, while the magnitude of the electrostatic force is reduced by differential charging, the electrostatic torque may be enhanced due to greater leverage by protruding components such as solar panels. If the forces and torques resulting from a fully conducting spacecraft are considered to be the expected forces and torques, then differential charging can lead to large deviations with respect to the actual forces and torques. This is important to consider when using estimated forces and torques for feedforward control during OSAM operations subject to electrostatic perturbations. Thus, identifying and measuring differential charging using the methods described in [40] and [41] are important to generate a better model of the interspacecraft electrostatic forces and torques.

VI. CONCLUSION

This work compares reduced-order spacecraft charging models with the motivation of accurately computing the electrostatic force and torque acting on two spacecraft during proximity operations. The simplest model uses a simple sphere with an effective radius based on the self-capacitance of the spacecraft to compute the resulting environmental currents. While this model is convenient for studying charging transients, the resulting surface area might not be very accurate and can lead to large errors in the computed environmental plasma and secondary currents. The highest-fidelity model divides the spacecraft surface into several facets. Not only does this approximate the total surface area of the spacecraft more accurately but it also allows for the consideration of a time-varying and orientation-dependent sunlit area and ram-side area, which affects the photoelectric current and under some conditions the plasma ion current, respectively.

The faceted model is used to compute the expected equilibrium potential in cislunar regions using lunar plasma data that correspond to a high-charging environment and assuming an eclipsed spacecraft. The highest risk of charging is found to be in the plasma sheet, with natural potentials between -10 and -6 kV, depending on the spacecraft's orientation with respect to the ion flow. Such high potentials lead to electrostatic perturbations that can affect OSAM operations. To compare the charging models, the electrostatic forces and torques are computed for various spacecraft's orientations using the ET debris reorbit scenario as an example. A dynamic simulation shows that for the spacecraft shapes used in this work, the equilibrium potential and the resulting force and torque can significantly vary between a faceted and a spherical model. These results suggest that it may be beneficial to detumble and maintain a constant debris orientation while reorbiting, as opposed to letting the debris tumble freely. Finally, the effect of differentially charged spacecraft on the intercraft electrostatic forces and torques is investigated. The results show that if the potential of the solar panel is different from the remaining spacecraft, the force and torque can differ significantly compared to a fully conducting spacecraft, depending on the potential and the spacecraft's orientation. In some cases, this can cause force components to switch from being repulsive to being attractive. That is, instead of being pushed away, the spacecraft may be pulled toward each other.

ACKNOWLEDGMENT

The authors would like to thank Kaylee Champion for her assistance with NASCAP simulations for the verification of the charging model and for the fruitful discussions.

REFERENCES

- [1] S. T. Lai, *Fundamentals of Spacecraft Charging*. Princeton, NJ, USA: Princeton Univ. Press, Oct. 2011.
- [2] R. C. Olsen, "Record charging events from applied technology satellite 6," *J. Spacecraft Rockets*, vol. 24, no. 4, pp. 362–366, 1987.
- [3] H. B. Garrett and A. C. Whittlesey, *Guide To Mitigating Spacecraft Charging Effects*. Hoboken, NJ, USA: Wiley, May 2012.
- [4] I. Katz, V. Davis, and D. Snyder, "Mechanism for spacecraft charging initiated destruction of solar arrays in GEO," in *Proc. 36th AIAA Aerosp. Sci. Meeting Exhib.*, Jan. 1998, pp. 1–5.
- [5] H. Brandhorst and J. Rodiek, "Improving space utilization by increasing solar array reliability," in *Proc. AIAA Space Conf. Exposit.*, Sep. 2007, pp. 1–5.
- [6] K. Wilson and H. Schaub, "Impact of electrostatic perturbations on proximity operations in high Earth orbits," *J. Spacecraft Rockets*, vol. 58, no. 5, pp. 1293–1302, Sep. 2021.
- [7] H. Schaub and D. F. Moorer Jr., "Geosynchronous large debris reorbiter: Challenges and prospects," *J. Astron. Sci.*, vol. 59, nos. 1–2, pp. 161–176, 2012.
- [8] H. Schaub and D. Stevenson, "Prospects of relative attitude control using Coulomb actuation," *J. Astron. Sci.*, vol. 60, nos. 3–4, pp. 258–277, Dec. 2013.
- [9] K. Wilson, Á. Romero-Calvo, and H. Schaub, "Constrained guidance for spacecraft proximity operations under electrostatic perturbations," *J. Spacecraft Rockets*, vol. 59, no. 4, pp. 1304–1316, Jul. 2022.
- [10] H. Schaub and Z. Sternovsky, "Active space debris charging for contactless electrostatic disposal maneuvers," *Adv. Space Res.*, vol. 53, no. 1, pp. 110–118, Jan. 2014.
- [11] J. A. Hughes and H. Schaub, "Electrostatic tractor analysis using a measured flux model," *J. Spacecraft Rockets*, vol. 57, no. 2, pp. 207–216, Mar. 2020.
- [12] J. Hammerl and H. Schaub, "Effects of electric potential uncertainty on electrostatic tractor relative motion control equilibria," *J. Spacecraft Rockets*, vol. 59, no. 2, pp. 552–562, Mar. 2022.
- [13] J. Hammerl and H. Schaub, "Debris attitude effects on electrostatic tractor relative motion control performance," in *Proc. AAS/AIAA Astrodyn. Spec. Conf.*, Aug. 2021, pp. 1–13.
- [14] J. Hughes and H. Schaub, "Space weather influence on electromagnetic geosynchronous debris perturbations using statistical fluxes," *Space Weather*, vol. 16, no. 4, pp. 391–405, Apr. 2018.
- [15] D. Stevenson and H. Schaub, "Multi-sphere method for modeling spacecraft electrostatic forces and torques," *Adv. Space Res.*, vol. 51, no. 1, pp. 10–20, Jan. 2013.
- [16] J. Hammerl and H. Schaub, "Coupled spacecraft charging due to continuous electron beam emission and impact," *J. Spacecraft Rockets*, vol. 61, no. 5, pp. 1258–1271, Sep. 2024.
- [17] V. A. Davis and M. J. Mandell, "NASCAP-2K version 4.3 scientific documentation," Kirtland Air Force Base, NM, USA, Tech. Rep. AFRL-RV-PS-TR-2017-0001, 2016.
- [18] J. Wang and D. E. Hastings, "Ionospheric plasma flow over large high-voltage space platforms. II: The formation and structure of plasma wake," *Phys. Fluids B, Plasma Phys.*, vol. 4, no. 6, pp. 1615–1629, Jun. 1992.
- [19] D. E. Hastings, "A review of plasma interactions with spacecraft in low Earth orbit," *J. Geophys. Res., Space Phys.*, vol. 100, no. A8, pp. 14457–14483, Aug. 1995.
- [20] J. A. Hughes and H. Schaub, "Heterogeneous surface multisphere models using method of moments foundations," *J. Spacecraft Rockets*, vol. 56, no. 4, pp. 1259–1266, 2019.
- [21] P. Lundgreen and J. R. Dennison, "Strategies for determining electron yield material parameters for spacecraft charge modeling," *Space Weather*, vol. 18, no. 4, pp. 1–13, Apr. 2020.
- [22] N. Murdoch, D. Izzo, C. Bombardelli, I. Carnelli, A. Hilgers, and D. Rodgers, "Electrostatic tractor for near Earth object deflection," in *Proc. 59th Int. Astron. Congr.*, vol. 29, 2008, pp. 1–11.
- [23] C. R. Seubert, L. A. Stiles, and H. Schaub, "Effective Coulomb force modeling for spacecraft in Earth orbit plasmas," *Adv. Space Res.*, vol. 54, no. 2, pp. 209–220, 2014.
- [24] B. C. Roberts, "SLS-SPEC-159: Cross-program design specification for natural environments (DSNE)," Nat. Aeronaut. Space Admin., Marshall Space Flight Center Redstone, Arsenal, AL, USA, Tech. Rep. SLS-SPEC-159, Revision G, 2019. [Online]. Available: <https://ntrs.nasa.gov/citations/20200000867>
- [25] J. S. Halekas, S. D. Bale, D. L. Mitchell, and R. P. Lin, "Electrons and magnetic fields in the lunar plasma wake," *J. Geophys. Res., Space Phys.*, vol. 110, no. A7, pp. 1–21, Jul. 2005.
- [26] N. F. Ness, "Interaction of the solar wind with the moon," in *Solar-Terrestrial Physics/1970: Part II*. Dordrecht, The Netherlands: Springer, 1970, pp. 159–205.
- [27] G. Schubert and B. R. Lichtenstein, "Observations of moon-plasma interactions by orbital and surface experiments," *Rev. Geophys.*, vol. 12, no. 4, p. 592, 1974.

- [28] M. H. Denton, M. F. Thomsen, H. Korth, S. Lynch, J. C. Zhang, and M. W. Liemohn, "Bulk plasma properties at geosynchronous orbit," *J. Geophys. Res., Space Phys.*, vol. 110, no. A7, pp. 1–17, Jul. 2005.
- [29] H. Schaub and J. L. Junkins, *Analytical Mechanics of Space Systems*, 4th ed. Reston, VA, USA: AIAA Education Series, 2018.
- [30] K. T. H. Wilson, "Remote electrostatic potential determination for spacecraft relative motion control," Doctoral thesis, Dept. Aerosp. Eng. Sci., Univ. Colorado Boulder, Boulder, CO, USA, 2021. [Online]. Available: <http://hanspeterschaub.info/Papers/grads/KieranWilson.pdf>
- [31] H. Schaub and L. E. Z. Jasper, "Orbit boosting maneuvers for two-craft Coulomb formations," *J. Guid., Control, Dyn.*, vol. 36, no. 1, pp. 74–82, Jan. 2013.
- [32] L. H. Brace, "Langmuir probe measurements in the ionosphere," *Geophys. Monograph-Amer. Geophys. Union*, vol. 102, pp. 23–36, Aug. 1998.
- [33] S. T. Lai and C. Miller, "Retarding potential analyzer: Principles, designs, and space applications," *AIP Adv.*, vol. 10, no. 9, Sep. 2020, Art. no. 095324.
- [34] M. Bengtson, J. Hughes, and H. Schaub, "Prospects and challenges for touchless sensing of spacecraft electrostatic potential using electrons," *IEEE Trans. Plasma Sci.*, vol. 47, no. 8, pp. 3673–3681, Aug. 2019.
- [35] M. T. Bengtson, K. T. Wilson, and H. Schaub, "Experimental results of electron method for remote spacecraft charge sensing," *Space Weather*, vol. 18, no. 3, pp. 1–12, Mar. 2020.
- [36] Á. Romero-Calvo, K. Champion, and H. Schaub, "Enabling ultraviolet lasers for touchless spacecraft potential sensing," *IEEE Trans. Plasma Sci.*, vol. 51, no. 9, pp. 2468–2481, Sep. 2023.
- [37] K. Wilson and H. Schaub, "X-ray spectroscopy for electrostatic potential and material determination of space objects," *IEEE Trans. Plasma Sci.*, vol. 47, no. 8, pp. 3858–3866, Aug. 2019.
- [38] K. T. Wilson, M. T. Bengtson, and H. Schaub, "X-ray spectroscopic determination of electrostatic potential and material composition for spacecraft: Experimental results," *Space Weather*, vol. 18, no. 4, pp. 1–10, Apr. 2020.
- [39] K. Wilson, J. Hammerl, and H. Schaub, "Using plasma-induced X-ray emission to estimate electrostatic potentials on nearby space objects," *J. Spacecraft Rockets*, vol. 59, no. 4, pp. 1402–1405, Jul. 2022.
- [40] Á. Romero-Calvo, J. Hammerl, and H. Schaub, "Touchless potential sensing of differentially charged spacecraft using secondary electrons," *J. Spacecraft Rockets*, vol. 59, no. 5, pp. 1623–1633, Sep. 2022.
- [41] J. Hammerl, A. López, Á. Romero-Calvo, and H. Schaub, "Touchless potential sensing of differentially charged spacecraft using X-rays," *J. Spacecraft Rockets*, vol. 60, no. 2, pp. 648–658, Mar. 2023.
- [42] S. M. L. Prokopenko and J. G. Laframboise, "High-voltage differential charging of geostationary spacecraft," *J. Geophys. Res., Space Phys.*, vol. 85, no. A8, pp. 4125–4131, Aug. 1980.
- [43] S. T. Lai and M. F. Tautz, "Aspects of spacecraft charging in sunlight," *IEEE Trans. Plasma Sci.*, vol. 34, no. 5, pp. 2053–2061, Oct. 2006.



Mr. Hammerl received the NASA FINESST fellowship in 2022.

Julian Hammerl received the bachelor's degree in mechanical engineering from Vienna University of Technology, Vienna, Austria, in 2020. He is currently pursuing the Ph.D. degree with the Autonomous Vehicle Systems (AVS) Laboratory, Aerospace Engineering Sciences Department, University of Colorado at Boulder, Boulder, CO, USA.

His research interests include spacecraft guidance and control, charged astrodynamics, active space debris removal, and remote sensing of electric potentials.



Hanspeter Schaub is a Professor and the Chair with the Aerospace Engineering Sciences Department, University of Colorado at Boulder, Boulder, CO, USA. He holds the Schaden Leadership Chair. He has over 28 years of research experience, of which four years are at Sandia National Laboratories, Albuquerque, NM, USA. He has been the ADCS Lead in the CICERO mission, the ADCS algorithm lead on a Mars mission, and supporting ADCS for a new asteroid mission. His research interests include astrodynamics, relative motion dynamics, charged spacecraft motion, and spacecraft autonomy. This has led to about 207 journal and 327 conference publications, as well as a fourth-edition textbook on analytical mechanics of space systems.

Dr. Schaub is a fellow of AIAA and AAS. He received the AIAA/ASEE Atwood Educator Award, AIAA Mechanics and Control of Flight Award, and the Collegiate Educator of the Year for the AIAA Rocky Mountain Section. He has been awarded the H. Joseph Smead Faculty Fellowship, the Provost's Faculty Achievement Award, the Faculty Assembly Award for Excellence in Teaching, and the Outstanding Faculty Advisor Award.